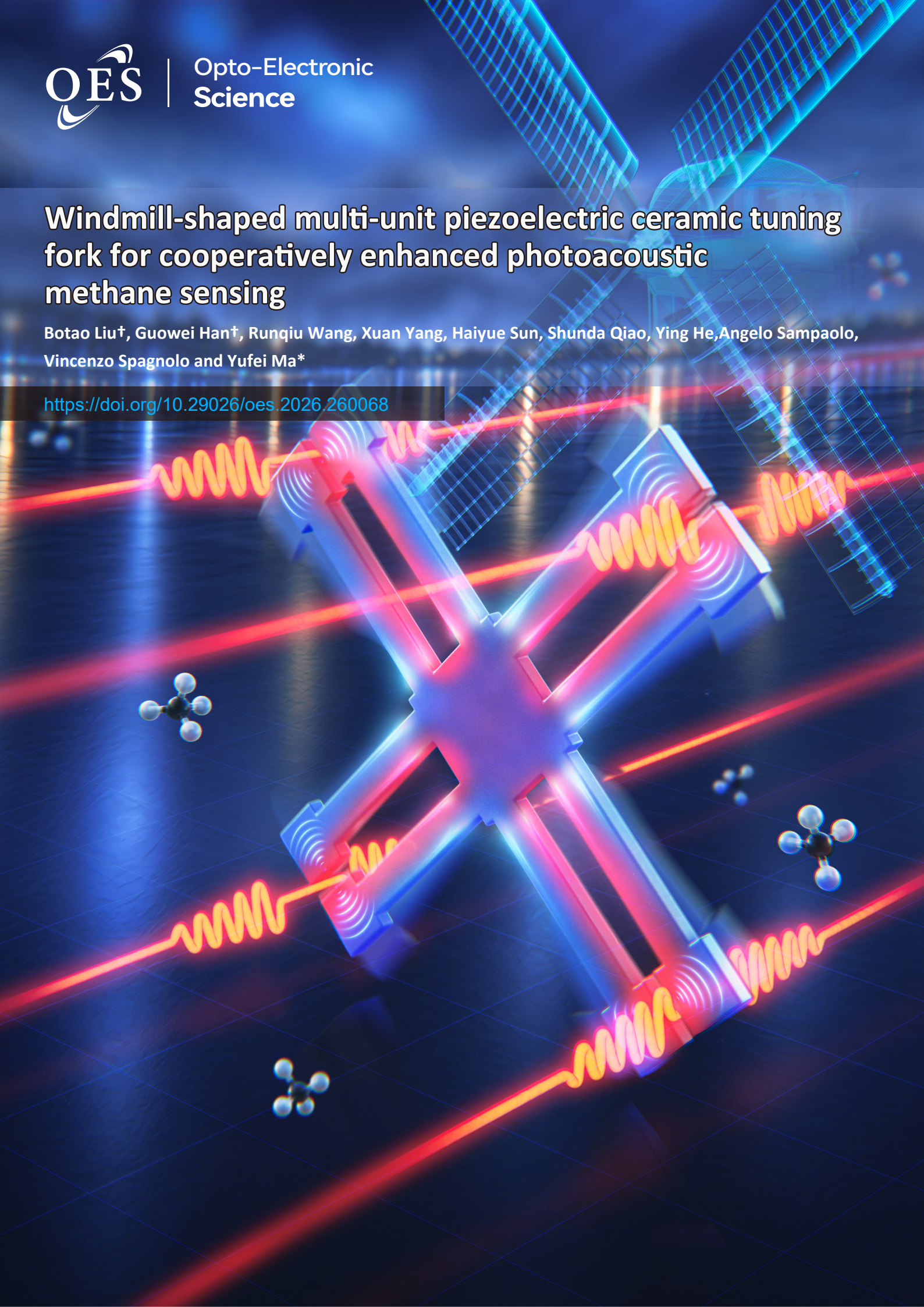
Opto-Electronic Science

Windmill-shaped multi-unit piezoelectric ceramic tuning fork for cooperatively enhanced photoacoustic methane sensing

Botao Liu†, Guowei Han†, Runqiu Wang, Xuan Yang, Haiyue Sun, Shunda Qiao, Ying He,Angelo Sampaolo, Vincenzo Spagnolo and Yufei Ma*

https://doi.org/10.29026/oes.2026.260068



Opto-Electronic Science

CN 51-1800/O4 ISSN (Print) 2097-0382 ISSN (Online) 2097-4000

Windmill-shaped multi-unit piezoelectric ceramic tuning fork for cooperatively enhanced photoacoustic methane sensing

Botao Liu, Guowei Han, Runqiu Wang, Xuan Yang, Haiyue Sun, Shunda Qiao, Ying He, Angelo Sampaolo, Vincenzo Spagnolo and Yufei Ma*

Citation: Liu BT, Han GW, Wang RQ et al. Windmill-shaped multi-unit piezoelectric ceramic tuning fork for cooperatively enhanced photoacoustic methane sensing. *Opto-Electron Sci* **5**, 260068 (2026).

https://doi.org/10.29026/oes.2026.260068

Received: 10 August 2026; Accepted: 24 September 2026; Published online: 22 October 2026

Related articles

Ppt-level volatile organic compounds detection via microsecond-pulse-enhanced mid-infrared photoacoustic

Senyu Wang, Liang Zhao, Hongyu Luo, et al

Opto-Electronic Science 2026, **5**(4): 260008 doi: 10.29026/oes.2026.260008

Imprinted high-*Q* polymer micro-ring resonator array for high-resolution photoacoustic tomography

Hyeonwoo Kim, Wei-Kuan Lin, Linyu Ni, et al

Opto-Electronic Advances 2026, **9**(6): 250215 doi: 10.29026/oea.2026.250215

Fast step heterodyne light-induced thermoelastic spectroscopy gas sensing based on a quartz tuning fork with high-frequency of 100 kHz

Yuanzhi Wang, Ying He, Shunda Qiao, et al

Opto-Electronic Advances 2026, **9**(1): 250150 doi: 10.29026/oea.2026.250150

Photoacoustic spectroscopy and light-induced thermoelastic spectroscopy based on inverted-triangular lithium niobate tuning fork

Junjie Mu, Guowei Han, Runqiu Wang, et al

Opto-Electronic Science 2025, **4**(12): 250035 doi: 10.29026/oes.2025.250035

More related articles in Opto-Electronic Journals Group website

Opto-Electronic Journals Group

https://www.oejournal.org

OE_Journal

@OptoElectronAdv

OES | Opto-Electronic Science

Article

October 2026, Vol. 5, No. 10

Open Access

Windmill-shaped multi-unit piezoelectric ceramic tuning fork for cooperatively enhanced photoacoustic methane sensing

Botao Liu[1,2†], Guowei Han[3†], Runqiu Wang[1,2], Xuan Yang[2], Haiyue Sun[1,2], Shunda Qiao[2], Ying He[2], Angelo Sampaolo[4], Vincenzo Spagnolo[4] and Yufei Ma[1,2*]

Abstract: In this work, a windmill-shaped multi-unit piezoelectric ceramic tuning fork (WMPCTF) is proposed for the first time and applied to highly sensitive methane (CH_4) detection based on piezoelectric ceramic-enhanced photoacoustic spectroscopy (PCPAS). The WMPCTF consists of four symmetrically distributed local tuning fork units that are structurally coupled to vibrate synchronously in a common resonance mode, enabling additive piezoelectric charge output. Finite-element simulations indicate that the total piezoelectric charge generated by the WMPCTF is 3.76 times that of the conventional PCTF. Experimental results confirm highly consistent resonance and photoacoustic piezoelectric responses among the four units. By combining a four-pass excitation path with four pairs of optimized acoustic microresonators (AmRs), the system achieves signal and signal-to-noise ratio enhancement factors of ~453 and ~394, respectively, relative to the one-pass WMPCTF configuration without AmRs. After increasing the optical power using a Raman fiber amplifier, the sensor exhibits an excellent linear concentration response and yields an SNR-derived minimum detection limit (MDL) of 19 ppb. Allan deviation analysis indicates a minimum detectable concentration of 0.87 ppb at an averaging time of ~760 s. Within the set of near-infrared tuning-fork photoacoustic sensors considered here, the proposed WMPCTF based PCPAS sensor shows highly competitive detection performance. This work provides a novel strategy for the cooperative enhancement of multi-unit piezoelectric response, multi-pass photoacoustic excitation, and acoustic resonance in photoacoustic sensing.

Keywords: piezoelectric ceramic tuning fork; photoacoustic spectroscopy; acoustic microresonator; CH_4 detection

DOI: 10.29026/oes.2026.260068 | CSTR: 32246.14.oes.2026.260068

Citation: Liu BT, Han GW, Wang RQ et al. Windmill-shaped multi-unit piezoelectric ceramic tuning fork for cooperatively enhanced photoacoustic methane sensing. *Opto-Electron Sci* **5**, 260068 (2026).

1 Introduction

Trace gas detection is essential for environmental monitoring[1–3], industrial safety[4–6], energy management[7–10], and atmospheric research[11–15]. Among various target gases, methane (CH_4) has attracted particular attention because of its pronounced greenhouse effect, energy value, and potential safety hazards. As the second most important anthropogenic greenhouse gas after carbon dioxide, CH_4 leakage during natural gas extraction, transportation, and storage not only contributes to climate change but also causes energy losses and generates explosion risks. Therefore, the development of sensitive and reliable methane detection techniques is of considerable importance for environmental protection and industrial applications[16–18]. Conventional CH_4 sensing methods, including gas chromatography[19], electrochemical sensors[20], semiconductor sensors[21], and catalytic combustion sensors[22], are widely used, but their limitations are technique-dependent: Chromatographic methods provide high analytical selectivity at the expense of instrument complexity and measurement time, whereas electrochemical, semiconductor, and catalytic sensors may exhibit cross-sensitivity, drift, or environmental dependence. Laser spectroscopic sensing exploits the characteristic absorption fingerprints of gas molecules, enabling highly selective,

Received: 10 August 2026

Accepted: 24 September 2026

Published online: 22 October 2026

[1]Zhengzhou Advanced Research Institute, Harbin Institute of Technology, Zhengzhou 450008, China; [2]National Key Laboratory of Laser Spatial Information, Harbin Institute of Technology, Harbin 150001, China; [3]Engineering Research Center for Semiconductor Integrated Technology, Institute of Semiconductors, Chinese Academy of Sciences, Beijing 100083, China; [4]PolySense Lab-Dipartimento Interateneo di Fisica, Politecnico di Bari, Via Amendola 173, Bari, Italy.

[†]These authors contributed equally to this work.

*Correspondence: YF Ma, E-mail: mayufei@hit.edu.cn

sensitive, and reliable trace gas measurements[23–30].

Quartz tuning fork (QTF)-based laser spectroscopic techniques have been widely investigated for compact and highly sensitive gas sensing[31–34]. According to their signal-generation mechanisms, these techniques mainly include light-induced thermoelastic spectroscopy (LITES) and quartz-enhanced photoacoustic spectroscopy (QEPAS)[35,36]. In LITES, a laser beam carrying gas absorption information irradiates the QTF surface, inducing periodic thermoelastic deformation that is subsequently converted into an electrical signal through the piezoelectric effect. However, a sufficiently long gas absorption path is generally required to obtain a sensitive LITES response, which increases the optical footprint and alignment complexity of the system[37–41]. In QEPAS, gas molecules absorb modulated laser radiation and generate photoacoustic waves through non-radiative relaxation. The photoacoustic waves excite the mechanical vibration of the QTF, and the resulting deformation is converted into an electrical signal through the piezoelectric effect. Since its introduction in 2002, QEPAS has become a widely investigated technique for trace gas sensing[42–44]. The compact dimensions, high quality factor, and narrow-band response of QTFs enable QEPAS systems with high sensitivity, strong immunity to environmental acoustic noise, and good long-term stability.

The QTF is the core piezoelectric transducer in a QEPAS system, and its electromechanical characteristics directly influence the overall sensing performance. Commercial 32.768 kHz QTFs were initially adopted because of their low cost and ready availability. Nevertheless, the low piezoelectric coefficient of quartz (d_{12}=2.3 pC/N) limits charge generation under weak acoustic excitation. In addition, the relatively high resonance frequency of a standard QTF shortens the acoustic energy accumulation time, whereas its narrow prong gap complicates optical alignment and increases susceptibility to optical-background interference. Improving the performance of tuning-fork-based photoacoustic transducers has therefore become an important research direction.

At the transducer level, current improvement strategies mainly involve structural optimization and material substitution of the tuning fork. Existing structural studies have primarily focused on tailoring the prong length, width, spacing, head geometry, and electrode configuration to reduce the resonance frequency, extend the acoustic energy accumulation time, improve stress distribution, and increase piezoelectric charge generation[45–53]. However, quartz is an anisotropic single-crystal material whose piezoelectric response strongly depends on the crystallographic orientation and vibration direction[54,55]. When QTF branches with identical geometries are aligned along different in-plane crystallographic directions, the correspondence between the mechanical stress components and the piezoelectric coefficient tensor changes, resulting in distinct surface-charge distributions and electrical outputs. This orientation dependence makes it difficult for branches arranged along different directions to maintain equivalent piezoelectric responses and consequently limits the structural design flexibility of quartz-based transducers.

Another effective approach is to replace quartz with piezoelectric materials possessing stronger electromechanical conversion capability[56]. Piezoelectric ceramics are polycrystalline ferroelectric materials composed of randomly oriented grains and ferroelectric domains[57]. After poling under a strong direct-current electric field, the domains become preferentially aligned, producing a pronounced macroscopic piezoelectric response. Owing to their high piezoelectric coefficients (>100 pC/N)[58,59], piezoelectric ceramics can generate larger electrical outputs than quartz under the same mechanical excitation. Moreover, when uniformly poled along the thickness direction, defined as the *z*-axis, piezoelectric ceramics exhibit approximately equivalent macroscopic electromechanical responses along the two orthogonal in-plane directions[60,61]. Therefore, branches extending along different in-plane directions can employ the same poling and electrode configurations while maintaining comparable piezoelectric responses. These characteristics provide a suitable material basis for developing tuning-fork transducers with greater geometric freedom and more extensive stress and charge-generation regions.

Based on these considerations, we introduce a windmill-shaped multi-unit piezoelectric ceramic tuning fork (WMPCTF) for the first time for piezoelectric ceramic-enhanced photoacoustic spectroscopy (PCPAS) CH_4 detection. Four symmetrically distributed tuning-fork units are mechanically coupled through a common central region and designed to operate synchronously in a single in-plane resonance mode. This architecture is intended to enlarge the spatially distributed stress and piezoelectric charge-generation regions while allowing the piezoelectric outputs of the four units to be collected additively. A folded four-pass optical path and four pairs of acoustic microresonators (AmRs) are then matched to the four local units to provide distributed photoacoustic excitation and acoustic enhancement. This resulting material-structure-acoustic co-design exploits both the high piezoelectric response and approximately equivalent in-plane electromechanical behavior of thickness-poled piezoelectric ceramics.

2 WMPCTF simulation and fabrication

The design concept of the WMPCTF is illustrated in Fig. 1. Inspired by the fourfold symmetric configuration of a windmill, four identical piezoelectric ceramic tuning fork units are arranged radially around a common central anchor at intervals of 90°. Unlike a conventional tuning fork, which contains only one pair of prongs and produces a local piezoelectric response S_0, the WMPCTF introduces four spatially distributed vibration and charge-generation regions without simply enlarging a single tuning fork. Within each local

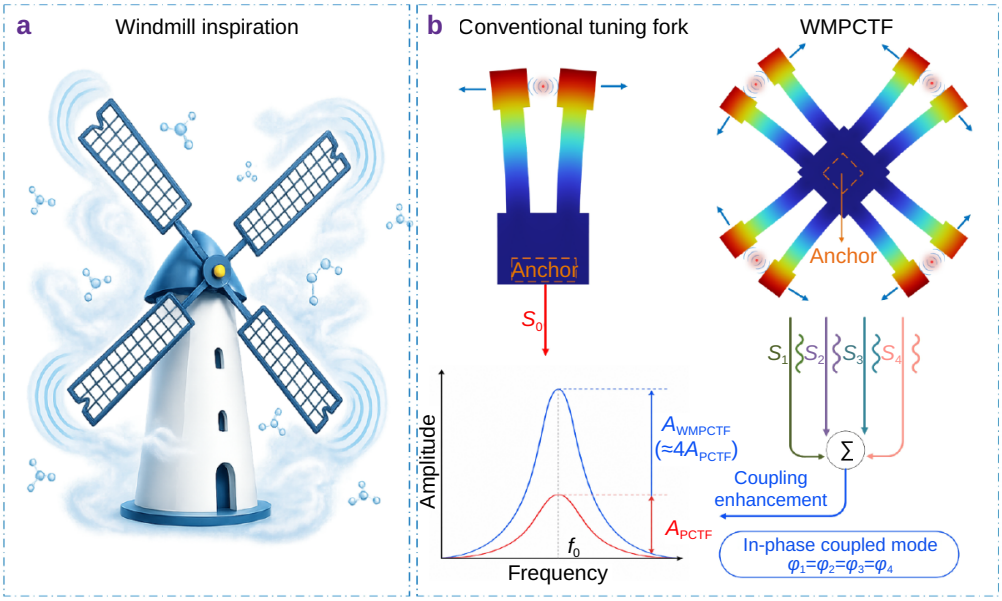


Fig. 1 | Design concept of the WMPCTF. (a) Windmill-inspired fourfold symmetric configuration. (b) Comparison between the conventional tuning fork and the proposed WMPCTF, illustrating the superposition of four local piezoelectric responses.

unit, the two prongs undergo anti-phase in-plane flexural vibration, while the four units are mechanically connected through the central region and operate synchronously in the target in-phase coupled mode. Four optical passes through the corresponding prong gaps generate the photoacoustic excitations S_1, S_2, S_3, and S_4. Owing to the approximately equivalent in-plane electromechanical responses of the thickness-poled piezoelectric ceramic, the four units can adopt identical geometries, poling conditions, and electrode configurations. By appropriately arranging the electrode polarities, the generated piezoelectric charges are additively collected, enabling the WMPCTF to combine spatially distributed photoacoustic excitation, coupled mechanical vibration, and synchronous electrical output within a compact planar structure.

For a piezoelectric ceramic tuning fork (PCTF) operating in the fundamental in-plane flexural mode, each prong can be approximately treated as a clamped-free beam. The fundamental resonance frequency of a single prong, denoted by f_s, can be expressed as

$$f_s = \frac{\beta_1^2 W}{2\pi\sqrt{12}L^2}\sqrt{\frac{E_{\text{eff}}}{\rho}}, \tag{1}$$

where L and W are the effective prong length and in-plane width, respectively; E_{eff} and ρ are the effective Young's modulus and density of the piezoelectric ceramic, respectively; and β_1=1.875 is the modal constant of the fundamental flexural mode. Equation (1) indicates that the resonance frequency is proportional to the prong width and inversely proportional to the square of the effective prong length. The collective vibration of the WMPCTF can be described using a simplified cyclic four-resonator model. Each local PCTF unit is represented by an effective mass m_e and stiffness k_e, while the mechanical interaction between adjacent units is represented by an equivalent coupling stiffness k_c. The coupled modal frequencies f_n can be expressed as

$$f_n = \frac{1}{2\pi}\sqrt{\frac{k_e + 2k_c\left[1-\cos\left(\frac{n\pi}{2}\right)\right]}{m_e}}, n = 0, 1, 2, 3\,. \tag{2}$$

In this model, the mode index n also determines the phase difference between adjacent local PCTF units. For the target in-phase coupled mode, n = 0, and the phase relationship becomes

$$\varphi_1 = \varphi_2 = \varphi_3 = \varphi_4\,, \tag{3}$$

where φ_i denotes the vibration phase of the i-th local PCTF unit. Thus, the four local PCTF units vibrate synchronously, providing the mechanical basis for the additive collection of their piezoelectric responses. Under the ideal cyclic coupling assumption, the relative deformation between adjacent units vanishes in this mode, and the coupling term in Eq. (2) becomes zero. In the actual WMPCTF, however, the central connection region and anchor geometry modify the effective modal stiffness and mass. Its resonance frequency can therefore be expressed as

$$f_{\text{WMPCTF}} \approx \frac{1}{2\pi}\sqrt{\frac{k_{\text{eff,W}}}{m_{\text{eff,W}}}}\,, \tag{4}$$

where $k_{\text{eff,W}}$ and $m_{\text{eff,W}}$ denote the effective modal stiffness and mass of the WMPCTF, respectively. The piezoelectric response of the WMPCTF originates from the bending stress induced by photoacoustic excitation. The four spatially distributed optical passes generate four photoacoustic

excitation regions corresponding to the four local PCTF units. For the i-th unit, the photoacoustic wave can be represented by an equivalent transverse force $F_{\mathrm{ac},i}$ acting on each prong of the local tuning-fork unit. The maximum longitudinal bending stress near the prong root can be approximated as

$$\sigma_{\max,i} = \frac{M_{\max,i}c}{I} = \frac{6F_{\mathrm{ac},i}L}{TW^2}, i = 1, 2, 3, 4 \ , \tag{5}$$

where $M_{\max,i} = F_{\mathrm{ac},i}L$ is the maximum bending moment; T is the thickness of the piezoelectric ceramic; $c = W/2$; $I = TW^3/12$ is the second moment of area associated with the in-plane bending of the prong along the width direction. Under identical optical excitation and structural conditions, the four equivalent photoacoustic forces and the resulting root stresses are approximately equal.

In the absence of an externally applied electric field, the direct piezoelectric effect can be expressed as

$$\boldsymbol{D} \approx \boldsymbol{d\sigma} \ , \tag{6}$$

where $\boldsymbol{D}$ is the electric displacement vector, $\boldsymbol{d}$ is the piezoelectric coefficient matrix, and $\boldsymbol{\sigma}$ is the stress tensor. Under this condition, the electric-field-dependent dielectric term in the full piezoelectric constitutive relation is neglected, and only the stress-induced electric displacement is considered. The charge collected by the electrode of the i-th local unit is therefore given by

$$q_i = \int_{S_{\mathrm{e},i}} \boldsymbol{D} \cdot \boldsymbol{n} \mathrm{d}S \approx \int_{S_{\mathrm{e},i}} (\boldsymbol{d\sigma}_i) \cdot \boldsymbol{n} \mathrm{d}S \ , \tag{7}$$

where $S_{\mathrm{e},i}$ is the electrode area and $\boldsymbol{n}$ is the outward normal vector of the electrode surface.

The piezoelectric ceramic is uniformly poled along the thickness direction, defined as the z-axis. For the two local PCTF units oriented along the x-direction, the dominant longitudinal stress is σ_1, and the thickness-direction electric displacement is mainly governed by the transverse piezoelectric coefficient d_{31}. For the other two units oriented along the y-direction, the dominant longitudinal stress is σ_2, and the corresponding response is governed by d_{32}. The local charge outputs can therefore be approximated as

$$\begin{cases} q_1,\ q_3 \approx \int_{S_{\mathrm{e},x}} d_{31}\sigma_1 \mathrm{d}S \\ q_2,\ q_4 \approx \int_{S_{\mathrm{e},y}} d_{32}\sigma_2 \mathrm{d}S \end{cases} . \tag{8}$$

For a uniformly thickness-poled polycrystalline piezoelectric ceramic, $d_{31} \approx d_{32}$. Therefore, under identical geometrical and photoacoustic excitation conditions, the four local PCTF units generate approximately equal charge amplitudes, denoted by q_0. Since the four charge responses have the same phase in the target coupled mode and the electrode polarities are configured for additive collection, the total charge output can be directly expressed as

$$q_{\mathrm{WMPCTF}} = q_1 + q_2 + q_3 + q_4 = 4q_0 \ . \tag{9}$$

Thus, under identical local photoacoustic excitation applied to each unit, the ideal total piezoelectric charge collected from the WMPCTF can approach four times that generated by a single PCTF unit. This fourfold limit describes additive charge superposition across four simultaneously excited local units; it should not be interpreted as an intrinsic fourfold transducer gain under fixed total optical excitation.

To further evaluate the WMPCTF structure, finite-element analysis (FEA) was conducted. The pressure acoustics, solid mechanics, and electrostatics interfaces were coupled to describe the generation of acoustic excitation, the structural vibration, and the piezoelectric response of the ceramic tuning forks. The principal geometrical dimensions of the PCTF and WMPCTF models are indicated in Fig. 2. The tuning-fork plane was defined as the x-y plane, with the z-axis along the thickness direction. For the quartz models, an ideal z-cut configuration without additional angular rotation was adopted, with the crystallographic coordinate system coincident with the global coordinate system. The longitudinal direction of the conventional QTF prongs was

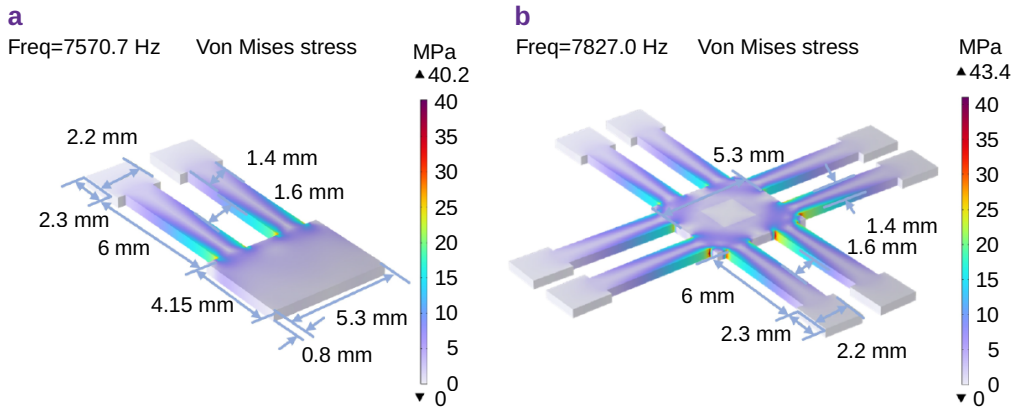


Fig. 2 | Geometrical dimensions and simulated von Mises stress distributions of (a) PCTF and (b) WMPCTF under line-source photoacoustic excitation at their respective resonance frequencies.

parallel to the crystallographic *y*-axis, while the four local units of the WMQTF were oriented along the ±*x* and ±*y* directions. For the piezoelectric ceramic models, the four local units were correspondingly oriented along the ±*x* and ±*y* directions, with the ceramic uniformly poled along the thickness (*z*) direction. The densities and relative dielectric constants were 2651 kg·m^{-3} and 4.51 for quartz and 7500 kg·m^{-3} and 1050 for the piezoelectric ceramic, respectively. Empirical quality factors of 10000 and 1500 were adopted to represent the overall resonator losses. The elastic stiffness and piezoelectric coefficients used in the simulations are provided in Supplementary Table S1. A line acoustic source was placed near the prong-tip region of the conventional PCTF, whereas four identical line acoustic sources were applied to the WMPCTF, with one source corresponding to each local tuning-fork unit along the four directions. Each line source passed through the center of the gap between the two hammer-shaped prong tips, with a length of 15 mm and an input power of 10 mW. The four sources in the WMPCTF were set with the same phase. Frequency-domain analysis was then performed, and the stress distributions were extracted at the corresponding resonance frequencies. As shown in Fig. 2, the resonance frequencies of the PCTF and WMPCTF were 7570.7 and 7827.0 Hz, respectively, with a difference of approximately 3.4%. For both structures, the maximum stress was concentrated at the prong roots, consistent with the bending characteristics of the tuning fork prongs. Under the same individual line-source power, the maximum stresses of the PCTF and WMPCTF were 40.2 and 43.4 MPa, respectively, corresponding to an increase of approximately 8.0% for the WMPCTF. According to Eq. (5), the maximum bending stress is mainly determined by the local photoacoustic force and the prong dimensions. Because the WMPCTF and PCTF have identical prong dimensions and are subjected to the same local excitation, their maximum stress levels are expected to be comparable. The simulation results show that each local tuning-fork unit in the WMPCTF exhibits a stress response comparable to that of the conventional PCTF, while the piezoelectric outputs from the four units can be synchronously and additively combined to produce a higher overall signal.

The frequency-dependent total absolute surface charges of quartz and piezoelectric ceramic materials in conventional and windmill-shaped multi-unit tuning fork configurations were further calculated to evaluate their piezoelectric responses, as shown in Fig. 3. For the comparison between quartz and piezoelectric ceramic, identical geometrical

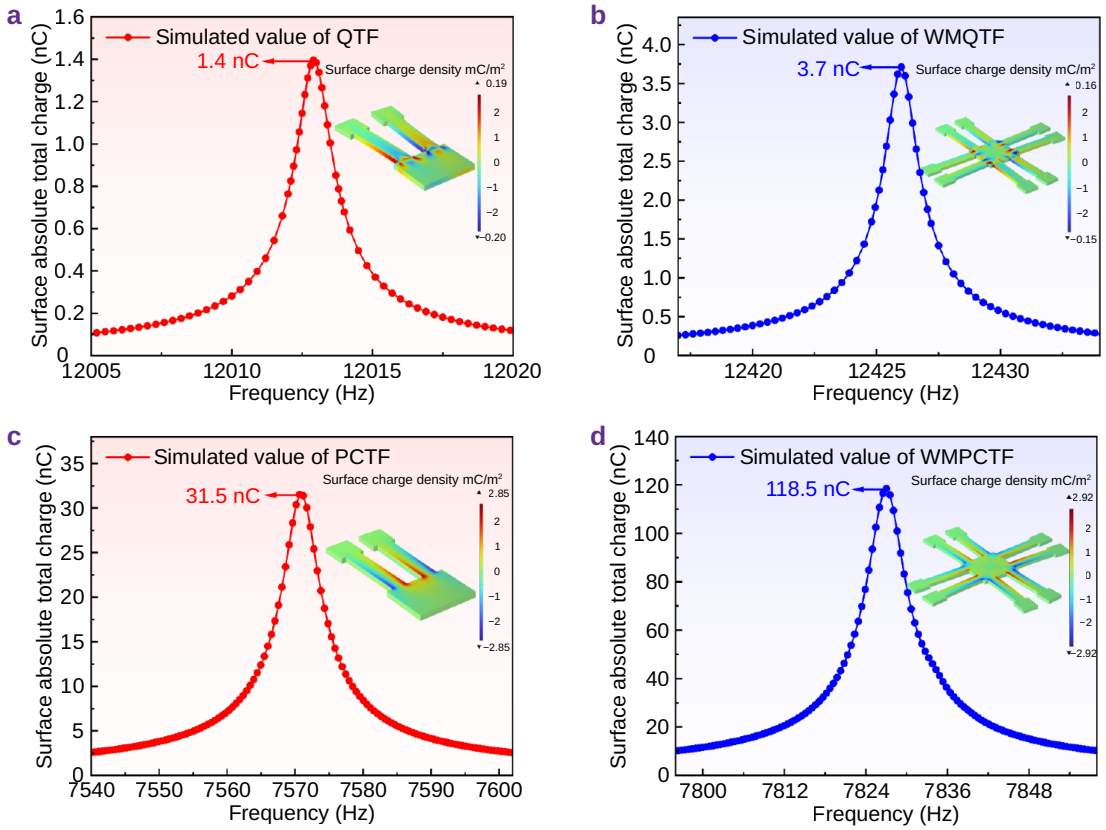


Fig. 3 | Simulated frequency-dependent total absolute surface charge of (a) QTF, (b) WMQTF, (c) PCTF, and (d) WMPCTF. The insets show the corresponding surface charge density distributions at resonance.

dimensions, excitation conditions, and boundary conditions were adopted. Here, the total absolute surface charge was obtained by integrating the absolute value of the surface charge density over the tuning-fork surfaces. As illustrated in the inset of Fig. 3(a), each surface of a single prong of the conventional QTF exhibits an approximately uniform charge polarity, while adjacent surfaces have opposite polarities; the corresponding surfaces of the other prong exhibit reversed polarities. In contrast, the inset of Fig. 3(c) shows that the two prongs of the PCTF have symmetric charge distributions, with the charges mainly concentrated on the major surfaces. On each surface, opposite polarities appear on the two sides of the prong centerline, while the upper and lower surfaces exhibit reversed charge signs. These differences originate from the distinct piezoelectric coefficient tensors and polarization configurations of quartz and piezoelectric ceramics. As shown in Fig. 3(a) and 3(c), the total surface absolute charges of the QTF and PCTF at resonance are 1.4 and 31.5 nC, respectively. The charge response of the PCTF is therefore approximately 22.5 times that of the QTF, demonstrating the stronger piezoelectric conversion capability of the ceramic material. Nevertheless, the larger dielectric permittivity of the piezoelectric ceramic also increases the device capacitance; therefore, the enhancement in practical output voltage is generally lower than that in total absolute surface charge.

The windmill configuration produces markedly different charge-distribution characteristics in quartz and piezoelectric ceramic materials. As shown in the inset of Fig. 3(b), the local tuning-fork pair of the windmill-shaped multi-unit quartz tuning fork (WMQTF) oriented perpendicular to the conventional charge-distribution direction exhibits a reconstructed charge pattern: the two sides of each prong carry opposite polarities, while the two prongs within the same local tuning fork exhibit mirror-symmetric distributions. The local tuning fork oriented in the opposite direction presents the same spatial distribution but reversed charge polarities. Such orientation-dependent and alternating charge distributions increase the difficulty of designing a unified electrode configuration for effective charge collection. In contrast, the inset of Fig. 3(d) shows that the four local tuning-fork units of the WMPCTF retain similar charge-distribution patterns after rotation owing to the approximately equivalent in-plane piezoelectric responses of the thickness-poled ceramic, facilitating consistent electrode coverage and additive charge collection. Comparing Fig. 3(a) and 3(b), the total absolute surface charge of the quartz structure at resonance increases from 1.4 to 3.7 nC, corresponding to a 2.64-fold enhancement. For the ceramic structures shown in Fig. 3(c) and 3(d), the total absolute surface charge at resonance increases from 31.5 to 118.5 nC, corresponding to a 3.76-fold enhancement, which approaches the ideal four-unit charge superposition predicted above. These 3.76-fold value is a charge-superposition result obtained with identical local acoustic sources applied to the four units and therefore quantifies the cooperative charge-collection capability of the architecture under this excitation condition. Together with the similar charge-distribution patterns after 90° rotation, this result supports the use of a common electrode strategy for additive readout and provides the theoretical basis for the subsequent experimental validation of the WMPCTF.

The fabrication procedure of the WMPCTF is illustrated in Fig. 4. Piezoelectric ceramic powders were first compacted into disk-shaped green bodies by dry pressing and subsequently densified through high-temperature sintering. The resulting ceramic substrates had a thickness of approximately 800 μm. Silver electrodes were then deposited on both major surfaces of the ceramic disks by screen printing. The electrode thickness was approximately 7 μm. A high direct-current electric field was applied across the thickness direction to align the ferroelectric domains and establish the macroscopic piezoelectric response. After poling, the designed electrode layouts were formed by selectively removing the silver layers using pulsed-laser ablation. A 532 nm picosecond laser with a pulse duration of 8 ps and a repetition rate of 100 kHz was used for electrode patterning. The laser power and scanning speed were set to 1 W and 500 mm/s, respectively, and two scanning passes were applied along the predefined electrode trajectories. Multiple PCTF and WMPCTF patterns were arranged on the ceramic substrates to enable batch processing. Finally, the devices were separated from the substrates by laser dicing along their predefined outer contours. A nanosecond laser with a power of 3 W was used for this process, with repeated scanning along the device contours until separation was achieved.

The fabricated tuning forks were then collected for electrode connection and subsequent characterization. The fabricated PCTF and WMPCTF devices after electrode patterning and laser dicing are shown in Fig. 5(a). Figure 5(b) presents the front- and back-side electrode configurations designed according to the simulated surface charge distributions, where the red and blue regions represent electrodes connected to different electrical terminals. By matching the electrode coverage and connection polarities with the surface charge distributions, the generated piezoelectric charges can be effectively collected, allowing the responses of the four local tuning-fork units in the WMPCTF to be additively combined.

3 Experimental setup

The experimental setup for methane detection is shown in Fig. 6(a). A single-mode distributed feedback (DFB) laser emitting at 1650.96 nm with output power of 28 mW was used to access a CH_4 absorption line. The spectral selectivity of the selected CH_4 absorption line and the potential interference from H_2O and CO_2 are further evaluated in Supplementary Fig. S1. A Raman fiber amplifier (RFA) was

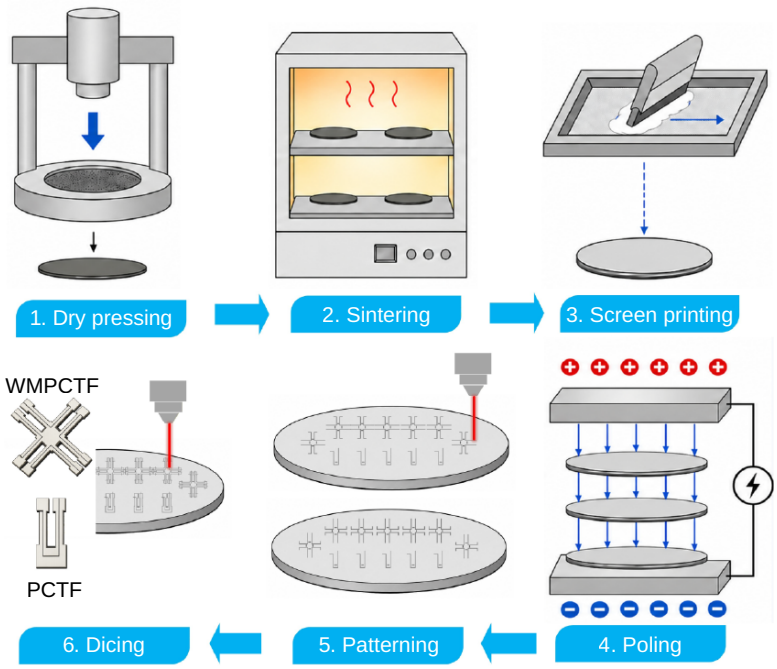


Fig. 4 | Fabrication process of the PCTF and WMPCTF.

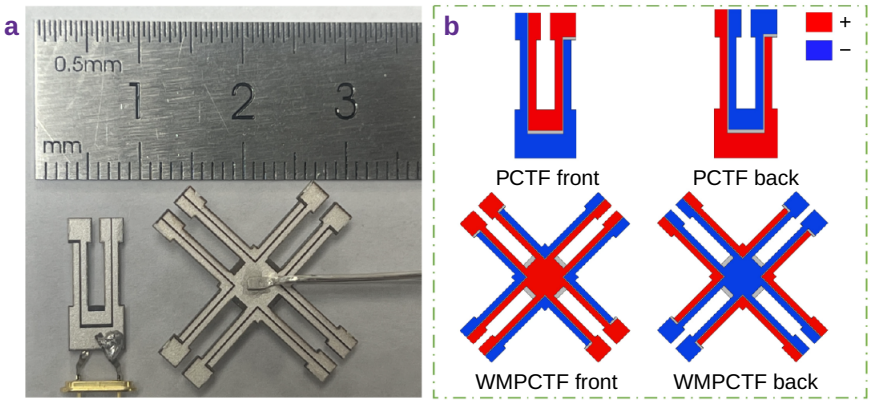


Fig. 5 | Fabricated tuning forks and electrode configurations. (a) Photographs of the PCTF and WMPCTF. (b) Front- and back-side electrode layouts, where red and blue indicate opposite electrical terminals.

introduced after the DFB laser to increase and adjust the excitation optical power up to 300 mW. Wavelength modulation spectroscopy combined with second-harmonic detection (WMS-2*f*) was employed. A low-frequency sawtooth signal generated by the function generator was used to scan the laser wavelength, while a sinusoidal signal from the lock-in amplifier provided wavelength modulation. The modulation frequency was set to half of the tuning fork resonance frequency, ensuring that the generated 2*f* photoacoustic component coincided with the mechanical resonance of the tuning fork. The lock-in amplifier was operated with a third-order low-pass filter, and the detection bandwidth was set to 405.5 mHz. After collimation, the laser beam entered the gas cell through an optical window. For clarity, Fig. 6(a) illustrates a representative beam passing through the prong gap of one local tuning fork unit. The modulated laser was periodically absorbed by CH_4 molecules, and the absorbed optical energy was converted into periodic heating through nonradiative relaxation. The resulting periodic thermal expansion and contraction of the gas generated pressure waves, which exerted a periodic photoacoustic force on the tuning fork prongs and excited their resonant vibration. The vibration was subsequently converted into an electrical signal through the piezoelectric effect, demodulated by the lock-in amplifier, and recorded by a computer. The CH_4 concentration was adjusted by mixing a 2% CH_4/N_2 standard gas with pure N_2 using two independent mass flow controllers (D08-2F, Beijing Sevenstar), each with a

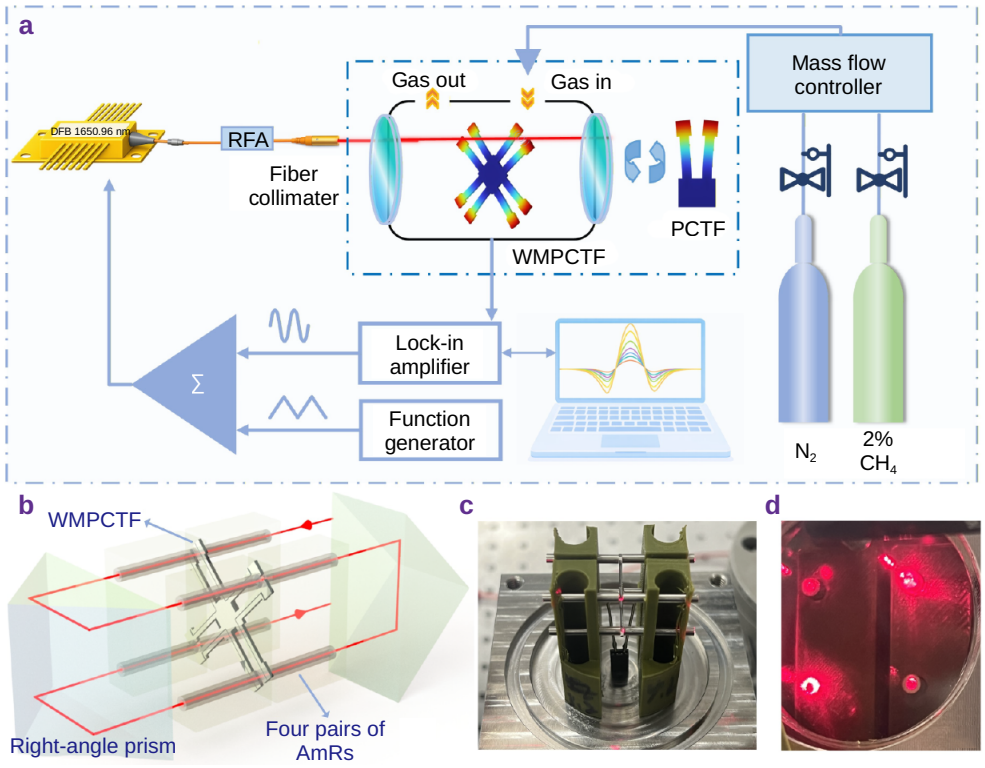


Fig. 6 | Experimental configuration of the WMPCTF based PCPAS sensor system. (a) Schematic of the experimental setup. (b) WMPCTF integrated with four pairs of AmRs. (c) Photograph of the assembled structure. (d) Laser spot distribution observed through the gas cell.

full-scale range of 120 sccm and a control accuracy of 1%. The total flow rate was maintained at 120 sccm, and the pressure in the gas cell was maintained at approximately 1 atm. The measurements were performed at room temperature. The cylindrical gas cell had a diameter of 55 mm and a height of 55 mm, corresponding to an internal volume of approximately 130.7 cm^3. The PCTF was tested under the same conditions for comparison.

As shown in Fig. 6(b), two pairs of right-angle prisms were arranged around the WMPCTF to construct a folded four-pass optical path, guiding the laser sequentially through the four prong gaps. Four pairs of acoustic microresonators (AmRs) were symmetrically positioned along the optical passes, with each pair aligned with one local tuning fork unit to enhance the corresponding photoacoustic excitation. This configuration generated four spatially distributed photoacoustic excitation regions within the gas cell. Figure 6(c) shows the assembled WMPCTF with four pairs of AmRs, while Fig. 6(d) presents the laser spot distribution observed through the gas cell, confirming the alignment of the four optical passes.

4 Experimental results and discussion

The resonance characteristics of the PCTF and WMPCTF were measured using an optically excited frequency sweep, as shown in Fig. 7(a). The squared signal amplitudes were normalized and fitted using Lorentzian profiles. The full width at half maximum (FWHM) bandwidths were extracted from the fitted resonance curves. The quality factor was calculated as $Q = f/w$, where f is the resonance frequency and w is the FWHM bandwidth. The PCTF exhibited a resonance frequency of 8039.6 Hz and a FWHM bandwidth of 5.16 Hz, corresponding to a quality factor Q of 1558. For the WMPCTF, the resonance frequency, FWHM bandwidth, and Q were 8370.09 Hz, 5.36 Hz, and 1561, respectively. The difference in resonance frequency arises from the changes in effective modal stiffness and effective modal mass introduced by the central connection and anchor region. The experimentally measured resonance frequencies were approximately 6%–7% higher than the simulated values. Since the resonance frequency is jointly determined by the effective stiffness and effective mass, the observed differences may result from deviations in the actual material properties, fabrication-induced dimensional variations, electrode layers, and differences between the idealized and actual anchoring conditions. The numerical model was primarily used to compare the modal characteristics and relative responses of different tuning-fork configurations rather than to exactly reproduce the absolute experimental resonance frequencies. Moreover, the Q of the WMPCTF was comparable to and slightly higher than that of the PCTF, indicating that the windmill configuration did not cause evident Q degradation.

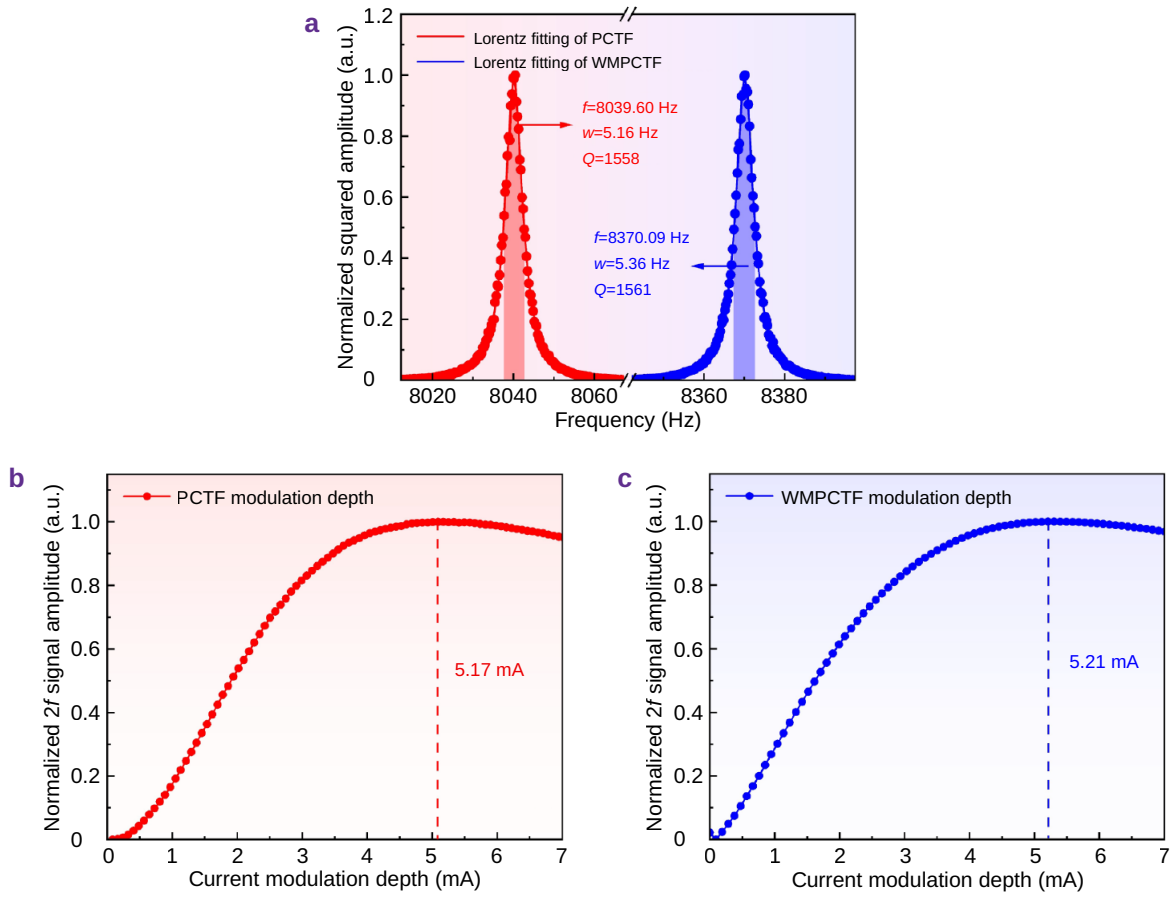


Fig. 7 | Resonance and modulation characteristics of the PCTF and WMPCTF. (a) Normalized squared frequency responses with Lorentzian fitting; current modulation depth optimization of (b) the PCTF and (c) the WMPCTF.

The modulation depth is a critical parameter affecting the signal amplitude and overall sensing performance. Therefore, the current modulation depths of the two systems were optimized by varying the modulation current. As shown in Fig. 7(b) and 7(c), the normalized 2*f* signals of the PCTF and WMPCTF reached their maximum values at modulation currents of 5.17 and 5.21 mA, respectively. The slightly higher optimal modulation depth of the WMPCTF is consistent with its higher modulation frequency.

The photoacoustic frequency responses of the PCTF and the four tine pairs of the WMPCTF were measured, as shown in Fig. 8(a). For TP1-TP4, the single-pass laser beam was sequentially passed through the gap between the prong tips of each tine pair, while the WMPCTF remained mechanically coupled and electrically connected through the same common electrodes. The four tine pairs are denoted as WMPCTF TP1, WMPCTF TP2, WMPCTF TP3, and WMPCTF TP4, respectively, where TP represents tine pair. The resonance frequency and peak signal amplitude of the PCTF were 8039.6 Hz and 6.74 μV, respectively. The resonance frequencies of WMPCTF TP1, TP2, TP3, and TP4 were 8370.2, 8370.4, 8370.2, and 8370.2 Hz, while the corresponding signal amplitudes were 6.62, 6.81, 6.67, and 6.70 μV, respectively. The frequency deviation among the four tine pairs was no more than 0.2 Hz, and their signal amplitudes were also close to each other and to that of the PCTF. These results demonstrate the good frequency consistency and response uniformity of the four local tuning fork units.

The signal enhancement provided by multiple optical passes was then investigated, as shown in Fig. 8(b). The one-pass and four-pass configurations are denoted as WMPCTF-1P and WMPCTF-4P, respectively. The peak 2*f* PCPAS signal amplitudes obtained with WMPCTF-1P and WMPCTF-4P were 6.71 and 20.52 μV, respectively, corresponding to a ~3-fold signal enhancement for the four-pass configuration. The corresponding 1σ noise levels were 20.25 and 21.81 nV, yielding SNRs of ~330 and ~940 for WMPCTF-1P and WMPCTF-4P, respectively, corresponding to a ~2.8-fold SNR enhancement for the four-pass configuration. The insets illustrate the laser paths passing through the prong tip gaps under the two configurations. The measured approximately threefold signal increase is consistent with effective cooperative collection from the four excited regions, although it does not represent a pure transducer-gain measurement because the four-pass

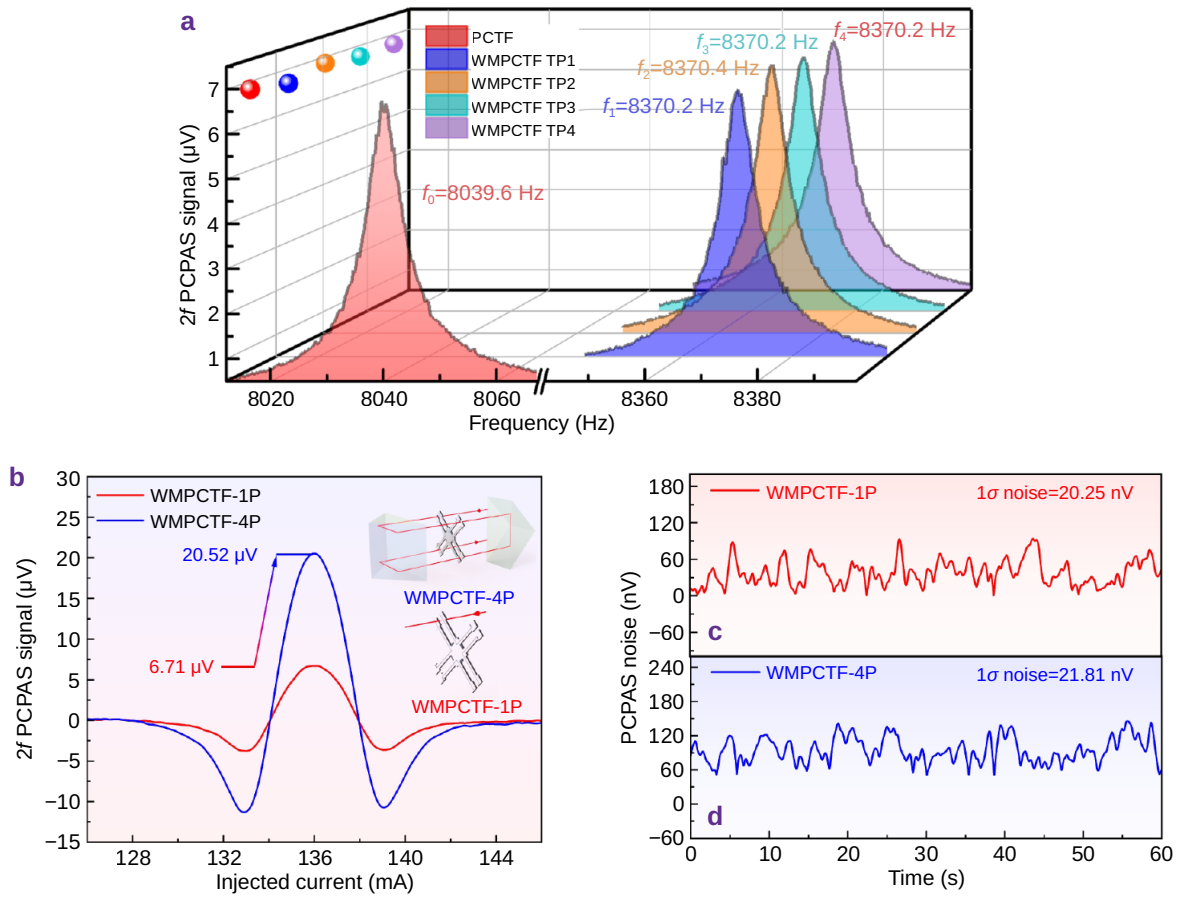


Fig. 8 | Photoacoustic response of the PCTF and WMPCTF. (a) Frequency responses of the PCTF and the four tine pairs (TP1–TP4) of the WMPCTF. (b) 2*f* CH_4-PCPAS signals under the one-pass (1P) and four-pass (4P) configurations, with the insets showing the corresponding optical paths; noise measurements of (c) WMPCTF-1P and (d) WMPCTF-4P.

configuration also redistributes the optical excitation among four local units. The deviation from the ideal fourfold charge-superposition limit is additionally influenced by reflection losses at the prisms, gas absorption, and expansion of the laser spot during successive passes.

To further enhance the photoacoustic force, AmRs were introduced into the WMPCTF-1P configuration. The AmRs form longitudinal acoustic standing waves and accumulate acoustic energy within the tubes, thereby increasing the acoustic pressure near the prong gaps and enhancing the photoacoustic force acting on the prongs. For the first order longitudinal resonance, the theoretical AmR length can be estimated as $L \approx \lambda_s/2 = v_s/(2f_{\mathrm{WMPCTF}})$, where λ_s and v_s are the acoustic wavelength and sound velocity in the gas, respectively. A sound velocity of approximately 343 m/s was adopted for the N_2-dominated gas mixture under room-temperature conditions, corresponding to an estimated AmR length of approximately 20.5 mm. The candidate tube lengths were selected around this theoretical value and further optimized experimentally. The effects of the AmR length and inner diameter on the 2*f* signal are shown in Fig. 9(a). The signal amplitude initially increased and then decreased with increasing tube length and inner diameter. The maximum signal amplitude of 1.24 mV was obtained at a tube length of 19 mm and an inner diameter of 1.0 mm. Based on the optimized dimensions, one and four pairs of AmRs were integrated with the WMPCTF, denoted as WMPCTF-1AmR and WMPCTF-4AmR, respectively. The two configurations are illustrated in the insets of Fig. 9(b). In WMPCTF-1AmR, the laser passes through one AmR pair and the corresponding prong gap. In WMPCTF-4AmR, two pairs of right angle prisms guide the laser sequentially through the four AmR pairs and the corresponding prong gaps. The peak 2*f* PCPAS signals of WMPCTF-1AmR and WMPCTF-4AmR were 1.24 and 3.04 mV, respectively. Compared with the 6.71 μV signal of WMPCTF-1P, the signal amplitudes were enhanced by factors of approximately 185 and 453, respectively. It is worth noting that after introducing the AmRs and achieving optimal acoustic coupling, the resonance frequency of the WMPCTF remained nearly unchanged as the number of AmR pairs increased from one to four, while only a slight decrease in *Q* was observed. The noise responses of WMPCTF-1AmR and WMPCTF-4AmR were measured over 60 s under pure N_2

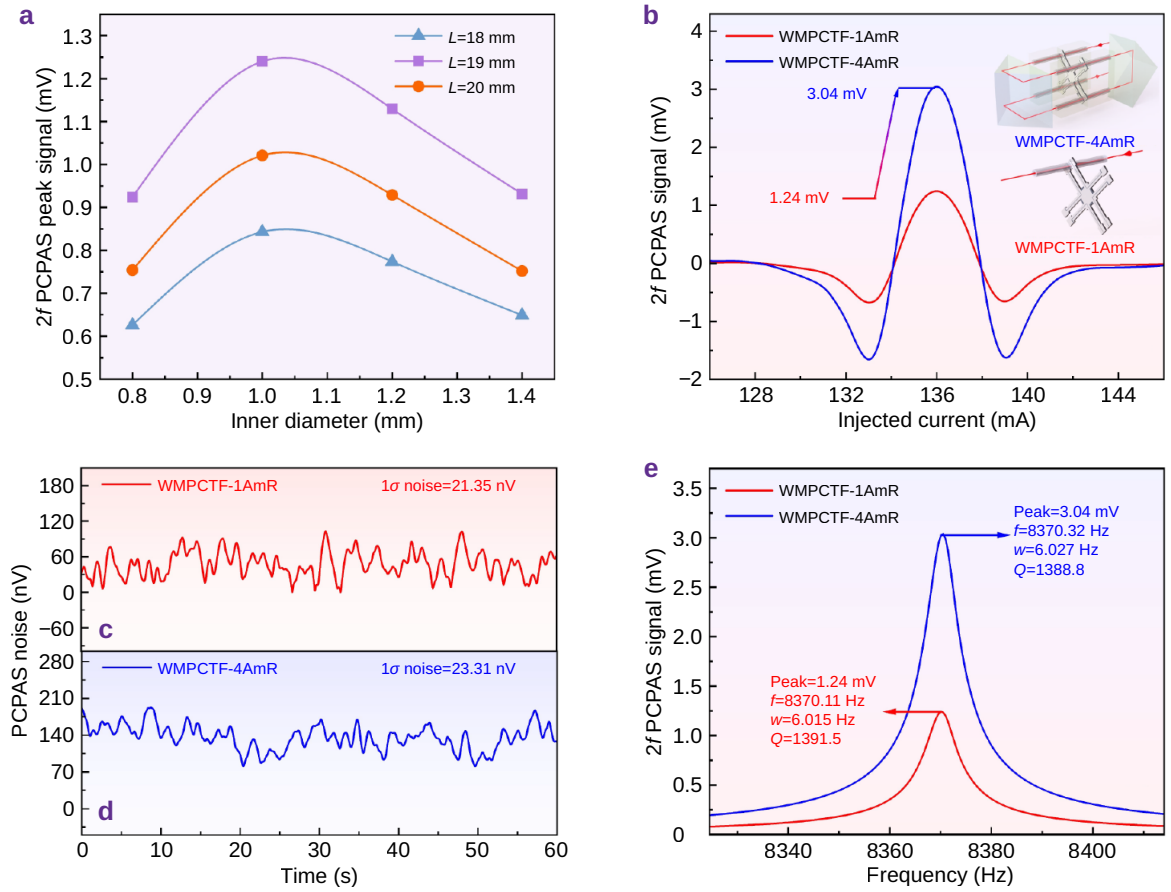


Fig. 9 | Optimization and performance of the WMPCTF with AmRs. (a) Dependence of the 2*f* CH_4-PCPAS peak signal on the AmR length and inner diameter. (b) 2*f* CH_4-PCPAS signals of WMPCTF-1AmR and WMPCTF-4AmR, with the insets showing the corresponding configurations; noise measurements of (c) WMPCTF-1AmR and (d) WMPCTF-4AmR. (e) Frequency responses of WMPCTF-1AmR and WMPCTF-4AmR.

conditions, as shown in Fig. 9(c) and 9(d). The corresponding 1σ noise levels were 21.35 and 23.31 nV, respectively. The calculated SNRs were 58080 and 130416, representing improvements of approximately 175 and 394 times compared with WMPCTF-1P. The SNR-derived MDL was calculated as $MDL = C/SNR$, where C is the corresponding CH_4 concentration. At a CH_4 concentration of 20000 ppm, the corresponding MDLs were calculated to be 0.34 and 0.15 ppm, respectively. The NNEA was calculated as $NNEA = \alpha_{min}P/B^{1/2}$, where α_{min}, P, and B are the minimum detectable absorption coefficient, optical power, and detection bandwidth, respectively. The corresponding NNEA values for WMPCTF-1AmR and WMPCTF-4AmR were 6.77×10^{-9} and 3.03×10^{-9} $Wcm^{-1}Hz^{-1/2}$, respectively. As shown in Fig. 9(e), the resonance frequencies of WMPCTF-1AmR and WMPCTF-4AmR are 8370.11 Hz and 8370.32 Hz, respectively, with corresponding Q values of 1391.5 and 1388.8. The slight frequency shift is attributed to the acoustic loading introduced by the AmRs, which causes a small perturbation to the resonance condition. Since the loss of the piezoelectric ceramic tuning fork is mainly dominated by intrinsic material dissipation, the additional acoustic loss introduced by the AmRs has only a limited influence on the Q value. When the number of AmR pairs increases from one to four, the additional AmRs provide extra acoustic excitation channels for the other local tuning-fork units, resulting in stronger acoustic driving of the WMPCTF. These AmRs exhibit similar frequency responses and couple to the same mechanical mode, so their contributions to the overall damping do not increase proportionally with the number of AmR pairs, resulting in only a negligible change in the Q value.

To further enhance the photoacoustic signal and improve the sensing performance, a RFA was employed to increase the excitation laser power. The 2*f* PCPAS signals measured at optical powers ranging from 50 to 300 mW are shown in Fig. 10(a). The signals maintained similar spectral profiles, while their amplitudes increased continuously with optical power. The peak values were extracted and linearly fitted, as shown in Fig. 10(b). A good linear relationship was obtained between the peak 2*f* signal amplitude and optical power, with an R^2 of 0.999. At an optical power of 300 mW, the signal amplitude reached ~28 mV, corresponding to an enhancement of ~9.2 times compared with that obtained

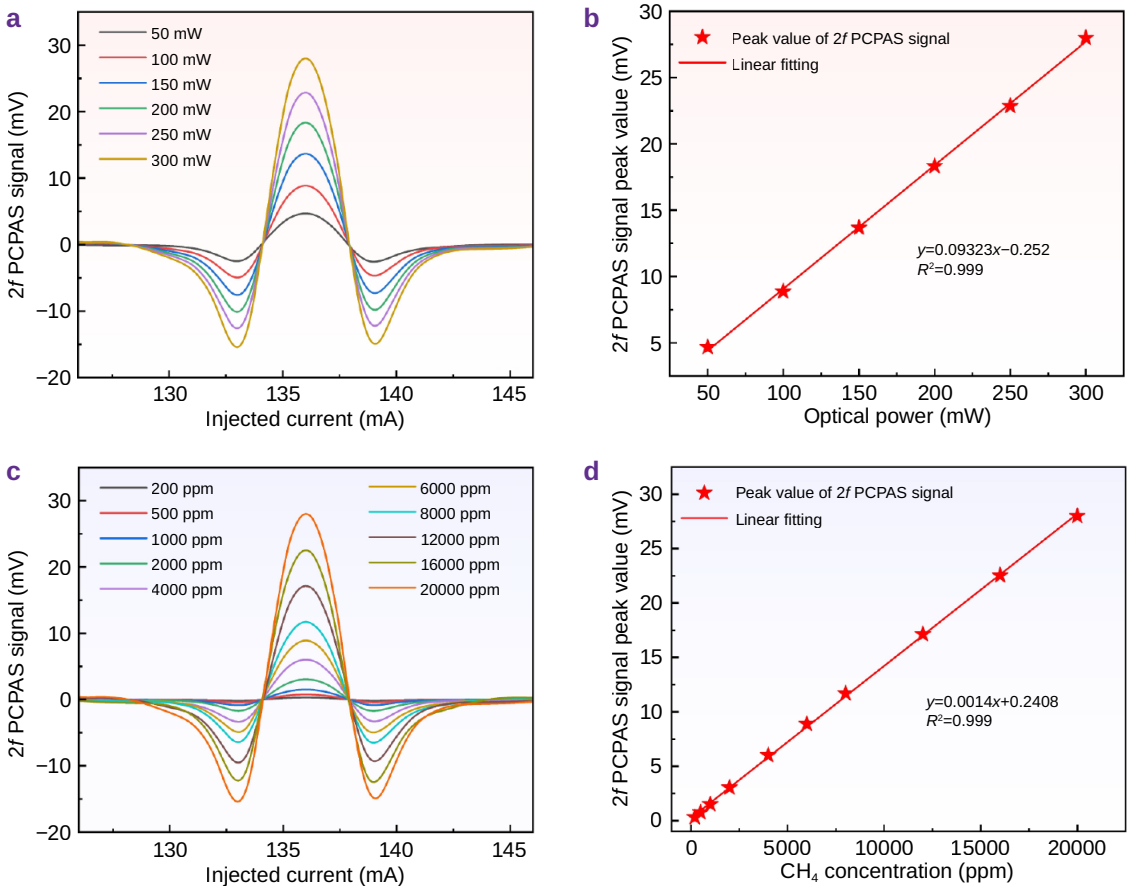


Fig. 10 | Optical power and concentration responses of the WMPCTF based CH_4-PCPAS sensor with the RFA. (a) 2*f* PCPAS signals at different optical powers. (b) Linear relationship between the peak 2*f* signal amplitude and optical power. (c) 2*f* PCPAS signals at different CH_4 concentrations. (d) Linear relationship between the peak 2*f* signal amplitude and CH_4 concentration.

without optical power amplification. The resulting power sensitivity was ~0.093 mV/mW.

The concentration response of the sensor was subsequently investigated at an optical power of 300 mW. The CH_4 concentration was adjusted from 200 to 20000 ppm by controlling the flow rates of the CH_4 standard gas and pure N_2. The measured 2*f* PCPAS signals at different CH_4 concentrations are presented in Fig. 10(c). As the CH_4 concentration increased, the signal amplitude increased continuously while the spectral profile remained nearly unchanged. The extracted peak values were linearly fitted as a function of CH_4 concentration, as shown in Fig. 10(d). The sensor exhibited an excellent linear response over the investigated concentration range, with an R^2 of 0.999 and a concentration sensitivity of 1.4 μV/ppm.

To determine the background noise, the sensor output was continuously recorded for 60 s under pure N_2 conditions, as shown in Fig. 11(a). Using the measured noise and the linear calibration response, the corresponding SNR-derived MDL is 19 ppb. The long-term stability of the WMPCTF based CH_4 sensor was further evaluated by continuously introducing pure N_2 into the gas cell and recording the sensor output for 3 h. The Allan deviation shown in Fig. 11(b) decreased with increasing averaging time and reached a minimum detection limit of 0.87 ppb at an approximate averaging time of 760 s. These measurements indicate low noise and good long-term stability of the WMPCTF based CH_4-PCPAS sensor. The SNR-derived MDL characterizes the detection capability under the specified measurement bandwidth, whereas the Allan-deviation-based value reflects the improved detection capability achieved through long-term averaging.

The CH_4 detection performance of the proposed sensor is compared with representative near-infrared QEPAS systems in Table 1. The selected studies operate at or near 1650.96 nm, allowing a more consistent wavelength-domain comparison. Within this comparison set, the proposed WMPCTF based CH_4-PCPAS sensor combines a high overall signal enhancement factor with a low SNR-derived MDL. The result arises from the cooperative contribution of multi-unit piezoelectric charge collection, four-pass photoacoustic excitation, and acoustic-resonator enhancement. To the best of our knowledge, the approximately 453 overall signal enhancement is among the highest reported for acoustic-

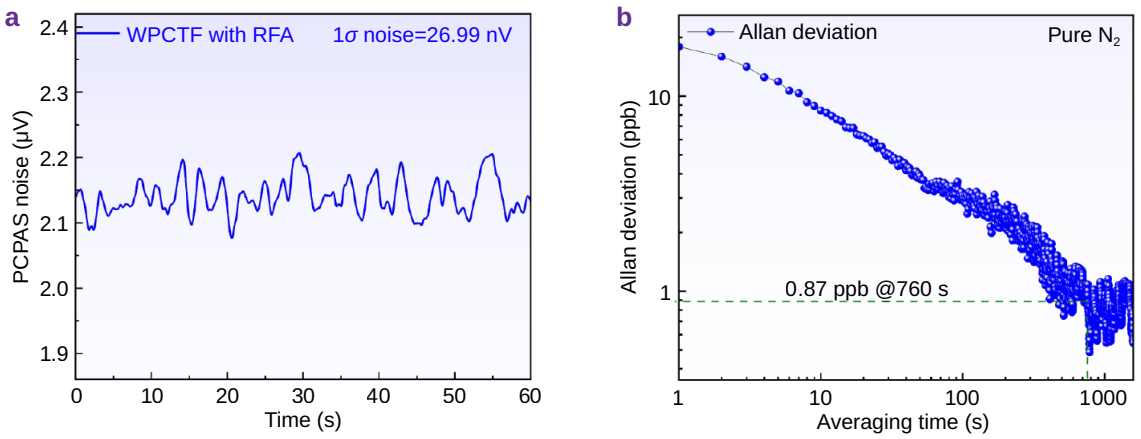


Fig. 11 | Noise and long-term stability of the WMPCTF based CH_4-PCPAS sensor. (a) Noise measured over 60 s under pure N_2 conditions. (b) Allan deviation calculated from a 3 h measurement under pure N_2 conditions.

Table 1 | Performance comparison of selected near-infrared CH_4 tuning-fork photoacoustic sensors based on QEPAS and PCPAS.

Reference	Method	Wavelength (nm)	Optical power (mW)	Overall signal enhancement factor	SNR-derived MDL (ppb)	Allan deviation-based MDL (ppb) (@ averaging time)
Ref.[62]	QEPAS	1650.96	16	13.3	14180	422 (@ 1000 s)
Ref.[63]	QEPAS	1650.96	27	149	711	19 (@ 4560 s)
Ref.[64]	QEPAS	1650.96	300	107	54.5	1.32 (@ 1000 s)
Ref.[65]	QEPAS	1650.96	296	–	94	11 (@ 150 s)
This work	PCPAS	1650.96	300	453	19	0.87 (@ 760 s)

resonator-enhanced tuning-fork PAS systems under the comparison definition adopted here.

5 Conclusions

In this work, a WMPCTF based PCPAS sensor was developed to overcome the single-local-response architecture of conventional tuning fork photoacoustic sensors. The windmill geometry enables four local tuning fork units to participate in a common resonance mode, providing spatially distributed photoacoustic excitation and additive piezoelectric charge collection within a single device. Theoretical analysis and finite-element simulations indicated that the four local units vibrate synchronously in the target in-phase mode, producing a total piezoelectric charge approximately 3.76 times that of the conventional PCTF under identical local excitations, while experiments confirmed highly consistent resonance and photoacoustic responses among the four tine pairs. Combining the four-pass optical path with four pairs of AmRs produced overall signal and SNR enhancement factors of ~453 and ~394, respectively. With 300 mW optical excitation provided by an RFA, the CH_4 sensor yielded an SNR-derived MDL of 19 ppb, while Allan deviation reached 0.87 ppb at an averaging time of approximately 760 s. To the best of our knowledge, these results represent the highest overall signal enhancement factor and the lowest CH_4 detection limit reported for an acoustic resonator-enhanced tuning fork PAS system. These results demonstrate that the cooperative integration of multi-unit piezoelectric transduction, distributed optical excitation, and acoustic resonance provides an effective strategy for enhancing tuning-fork-based photoacoustic gas sensing.

References

1. Lin XN, Lei FC, Liang X et al. Quantitative detection of trace nanoplastics (down to 50 nm) via surface-enhanced Raman scattering based on the multiplex-feature coffee ring. *Opto-Electron Adv* **8**, 240260 (2025).
2. Ma HX, Cai JZ, Qiao SD et al. Dual-gas light-induced thermoelastic spectroscopy sensor based on mixed-frequency heterodyne demodulation. *Light Adv Manuf* **7**, 54 (2026).
3. Pei ZY, Ji C, Shao MR et al. Enrichment strategies in surface-enhanced Raman scattering: theoretical insights and optical design for enhanced light-matter interaction. *Opto-Electron Sci* **4**, 250015 (2025).
4. Huang YK, He Y, Qiao SD et al. Intelligent algorithm-assisted indirect absorption spectroscopy for trace gas sensing. *Sensors* **26**, 4054 (2026).
5. Liu XN, Qiao SD, He Y et al. High-stability and fast calibration-free temperature measurement based on light-induced thermoelastic spectroscopy. *Ultrafast Sci* **5**, 0083 (2025).
6. Sun HY, He Y, Qiao SD et al. Highly sensitive and real-simultaneous CH_4/C_2H_2 dual-gas LITES sensor based on Lissajous pattern multi-pass cell. *Opto-Electron Sci* **3**, 240013 (2024).
7. Ma HX, Qiao SD, He Y et al. Orthogonal phase modulation and Lissajous mode decoupling in light-induced thermoelastic spectroscopy for real-time multi-component gas sensing. *Rep Prog Phys*

89, 067902 (2026).
8. Cai T, Valecha P, Tran V et al. Detection of Li-ion battery failure and venting with carbon dioxide sensors. *eTransportation* **7**, 100100 (2021).
9. Liu BY, Qiao SD, He Y et al. Single off-beam exciting dual-quartz-tuning-fork resonance-enhanced QEPAS trace gas sensing. *Chin Opt Lett* **23**, 103001 (2025).
10. Lyu ZH, Ma HX, Liu BY et al. Research progress on quartz-enhanced photoacoustic spectroscopy. *J Infrared Millim Waves* (2026). http://doi.org/10.11972/j.issn.1001-9014.JIMW.2026170.
11. Wen DYT, Zhao HT, Liu XF et al. Quantitative detection of water/ice in typical lunar minerals using Raman spectroscopy. *J Infrared Millim Waves* **44**, 192–202 (2025).
12. Giglio M, Zifarelli A, Sampaolo A et al. Broadband detection of methane and nitrous oxide using a distributed-feedback quantum cascade laser array and quartz-enhanced photoacoustic sensing. *Photoacoustics* **17**, 100159 (2020).
13. Yang X, Zhang C, Qiao SD et al. Non-resonant quartz-enhanced photoacoustic spectroscopy. *Chin Opt Lett* **23**, 093002 (2025).
14. Huang YK, Sun HY, Qiao SD et al. Self-supervised deep learning for denoising in light-induced thermoelastic spectroscopy using 2D homologous *2f* spectral matrices. *Laser Photonics Rev*, e71785 (2026). http://doi.org/10.1002/lpor.71785.
15. Mu JJ, He Y, Qiao SD et al. Antenna-inspired bionic lithium niobate tuning fork for multi-component light-induced thermoelastic spectroscopy sensing. *Laser Photonics Rev*, e71876 (2026). http://doi.org/10.1002/lpor.71876.
16. Menduni G, Zifarelli A, Kniazeva E et al. Measurement of methane, nitrous oxide and ammonia in atmosphere with a compact quartz-enhanced photoacoustic sensor. *Sens Actuators B Chem* **375**, 132953 (2023).
17. Twomey CF, Biagi G, Ruth AA et al. Side-polished fiber evanescent wave quartz-enhanced photoacoustic spectroscopy employing dielectric coatings for evanescent field enhancement. *Photoacoustics* **46**, 100782 (2025).
18. Zhao RJ, Yang X, Liu BT et al. Highly sensitive photoacoustic detection of methane based on a rhombic dual-channel differential photoacoustic cell. *Laser Part Beams* **44**, 20009 (2026).
19. van den Broek J, Abegg S, Pratsinis SE et al. Highly selective detection of methanol over ethanol by a handheld gas sensor. *Nat Commun* **10**, 4220 (2019).
20. Andre RS, Mercante LA, Facure MHM et al. Recent progress in amine gas sensors for food quality monitoring: novel architectures for sensing materials and systems. *ACS Sens* **7**, 2104–2131 (2022).
21. Tang YT, Zhao YN, Liu H. Room-temperature semiconductor gas sensors: challenges and opportunities. *ACS Sens* **7**, 3582–3597 (2022).
22. Dippong T, Levei EA, Cadar O. Recent advances in synthesis and applications of MFe$_2$O$_4$ (M = Co, Cu, Mn, Ni, Zn) nanoparticles. *Nanomaterials* **11**, 1560 (2021).
23. Li XF, Li JC, Ni X et al. Direct detection with an optimal transfer function: toward the electrical spectral efficiency of coherent homodyne detection. *Opto-Electron Sci* **4**, 240020 (2025).
24. Liu C, Xu MM, Hu M et al. CW DFB-QCL-based system for H_2O_2 detection using multi-pass tunable diode laser absorption spectroscopy. *Chin Opt Lett* **23**, 083001 (2025).
25. Nie QX, Peng YB, Chen QH et al. Agile cavity ringdown spectroscopy enabled by moderate optical feedback to a quantum cascade laser. *Opto-Electron Adv* **7**, 240077 (2024).
26. Nie QX, Wang Z, Ren W. Cavity-enhanced absorption spectroscopy with continuous and fast wavelength tuning. *Chin Opt Lett* **23**, 121201 (2025).
27. Qiao SD, He Y, Sun HY et al. Ultra-highly sensitive dual gases detection based on photoacoustic spectroscopy by exploiting a long-wave, high-power, wide-tunable, single-longitudinal-mode solid-state laser. *Light Sci Appl* **13**, 100 (2024).
28. Song YS, Ma HX, Qiao SD et al. Stable cavity ring-down spectroscopy enabled by intracavity injection with real-time PID feedback locking for reliable acetylene sensing. *Sens Actuators B Chem* **464**, 140199 (2026).
29. Xie ZL, Meng C, Yue DH et al. Tip-enhanced Raman scattering of glucose molecules. *Opto-Electron Sci* **4**, 240027 (2025).
30. Yang X, He Y, Zhang C et al. Skylark vocalization-inspired photoacoustic spectroscopy dual-component sensor based on a double-helix Helmholtz photoacoustic cell. *Sens Actuators B Chem* **467**, 140602 (2026).
31. Qiao SD, Liu XN, Lang ZT et al. Quartz-enhanced laser spectroscopy sensing. *Light Sci Appl* **15**, 5 (2026).
32. Sun HY, Qiao SD, He Y et al. High-speed and high-sensitivity multi-gas detection based on parallel heterodyne LITES sensor. *Light Sci Appl* **15**, 295 (2026).
33. Wang YZ, He Y, Qiao SD et al. Fast step heterodyne light-induced thermoelastic spectroscopy gas sensing based on a quartz tuning fork with high-frequency of 100 kHz. *Opto-Electron Adv* **9**, 250150 (2026).
34. Liu BY, Qiao SD, Lv ZH et al. On-off-beam differential resonance quartz-enhanced photoacoustic spectroscopy gas sensing technology. *Opt Lett* **51**, 3337–3340 (2026).
35. Ma HX, Qiao SD, He Y et al. Overtone acoustic feedback enhanced light-induced thermoelastic spectroscopy sensing. *Photonics Res* **14**, 683–689 (2026).
36. Qiao SD, Lv ZH, Ma HX et al. "1"-shaped acoustic cascaded resonator enhanced light-induced thermoelastic spectroscopy gas sensing. *Opt Lett* **51**, 3128–3131 (2026).
37. Liu YH, Qiao SD, Fang C et al. A highly sensitive LITES sensor based on a multi-pass cell with dense spot pattern and a novel quartz tuning fork with low frequency. *Opto-Electron Adv* **7**, 230230 (2024).
38. Ma HX, Liu BT, Qiao SD et al. A high-sensitivity light-induced thermoelastic spectroscopy sensor based on dual-path synergistic coupling method. *Laser Photonics Rev* **20**, e71169 (2026).
39. Ma YF, Sun XR, Sun HY et al. An ultra-highly sensitive LITES sensor based on multi-pass cell with ultra-dense spot pattern designed by multi-objective algorithm. *PhotoniX* **6**, 26 (2025).
40. Qiao SD, Lang ZT, He Y et al. Calibration-free measurement of absolute gas concentration and temperature via light-induced thermoelastic spectroscopy. *Adv Photonics* **7**, 066007 (2025).
41. Sun HY, Qiao SD, He Y et al. Parts-per-quadrillion level gas molecule detection: CO-LITES sensing. *Light Sci Appl* **14**, 180 (2025).
42. Qiao SD, Liu BY, Lv ZH et al. Elliptical acoustic resonator-based dual-quartz-enhanced photoacoustic spectroscopy sensing. *Anal Chem* **98**, 5707–5714 (2026).
43. Patimisco P, Scamarcio G, Tittel FK et al. Quartz-enhanced photoacoustic spectroscopy: a review. *Sensors* **14**, 6165–6206 (2014).
44. Zheng HD, Dong L, Sampaolo A et al. Single-tube on-beam quartz-enhanced photoacoustic spectroscopy. *Opt Lett* **41**, 978–981 (2016).
45. Mu JJ, Han GW, Wang RQ et al. Photoacoustic spectroscopy and light-induced thermoelastic spectroscopy based on inverted-triangular lithium niobate tuning fork. *Opto-Electron Sci* **4**, 250035 (2025).
46. Mu JJ, He Y, Qiao SD et al. Photoacoustic spectroscopy sensing based on an annular quartz tuning fork. *Sens Actuators B Chem* **463**, 140085 (2026).
47. Qiao SD, Lv ZH, Liu BY et al. Asymmetric tongs induced frequency splitting achieving simultaneous two-component gas sensing with a single quartz tuning fork in two independent resonant modes. *ACS*

Sens **11**, 7104–7114 (2026).
48. Wang RQ, Guan XY, Qiao SD et al. Ultrahigh sensitive LITES sensor based on a trilayer ultrathin perfect absorber coated T-head quartz tuning fork. *Laser Photonics Rev* **19**, 2402107 (2025).
49. Wang RQ, Qiao SD, He Y et al. Highly sensitive laser spectroscopy sensing based on a novel four-prong quartz tuning fork. *Opto-Electron Adv* **8**, 240275 (2025).
50. Zheng HD, Lin HY, Dong L et al. Influence of tuning fork resonance properties on quartz-enhanced photoacoustic spectroscopy performance. *Sensors* **19**, 3825 (2019).
51. Wu Q, Lv HH, Lin LQ et al. Clamp-type quartz tuning fork enhanced photoacoustic spectroscopy. *Opt Lett* **47**, 4556–4559 (2022).
52. Lin HY, Zheng HD, Zhu WG et al. Multifunctional lithium niobate platform for photodetection and photoacoustic and thermoelastic gas sensing. *Nat Commun* **17**, 2296 (2026).
53. Liu BT, Han GW, He Y et al. Owl-inspired dual-ended asymmetric lithium niobate tuning fork for high-sensitivity dual-gas laser spectroscopic sensing. *Photonics Res* **14**, 4579–4595 (2026).
54. Lamberson L, Ramesh KT. Dynamic electromechanical behavior of single-crystal *α*-quartz. *Int J Impact Eng* **110**, 338–345 (2017).
55. Yang G, Huang XH, Tan K et al. Study of force-frequency characteristics in AT-Cut strip quartz crystal resonators with different rotation angles. *Sensors* **23**, 2996 (2023).
56. Liu BT, Han GW, He Y et al. Piezoelectric ceramic tuning fork enhanced laser spectroscopic sensing. *Laser Photonics Rev* **20**, e71331 (2026).
57. Saito Y, Takao H, Tani T et al. Lead-free piezoceramics. *Nature* **432**, 84–87 (2004).
58. Someno S, Nagata H, Takenaka T. High-temperature and high-power piezoelectric characteristics of $(Bi_{0.5}Na_{0.5})TiO_3$-based lead-free piezoelectric ceramics. *J Ceram Soc Jpn* **122**, 406–409 (2014).
59. Tominaga T, Takagi Y, Nagata H et al. Doping effects for high-power piezoelectric properties on $Ba(Zr,Ti)O_3$-$(Ba,Ca)TiO_3$-based lead-free piezoelectric ceramics. *J Ceram Soc Jpn* **128**, 447–452 (2020).
60. Jayendiran R, Arockiarajan A. Micromechanical modeling and experimental characterization of 1–3 piezocomposites subjected to electromechanical loads. *Int J Eng Sci* **81**, 15–32 (2014).
61. Su Y, Weng GJ. Microstructural evolution and overall response of an initially isotropic ferroelectric polycrystal under an applied electric field. *Mech Mater* **41**, 1179–1191 (2009).
62. Zhang C, Qiao SD, He Y et al. Double resonant quartz-enhanced photoacoustic spectroscopy with a spherical resonator. *Opt Lett* **50**, 3776–3779 (2025).
63. Liang TT, Qiao SD, Chen YJ et al. High-sensitivity methane detection based on QEPAS and H-QEPAS technologies combined with a self-designed 8.7 kHz quartz tuning fork. *Photoacoustics* **36**, 100592 (2024).
64. Chen YJ, Ma HX, Qiao SD et al. Rapid ppb-level methane detection based on quartz-enhanced photoacoustic spectroscopy. *Anal Chem* **97**, 6780–6787 (2025).
65. Zatorska M, Gomółka G, Nikodem M. Near-infrared quartz-enhanced photoacoustic spectroscopy system for ppb-level methane detection. *Opt Continuum* **2**, 266–273 (2023).

Acknowledgements

This work was supported by the National Natural Science Foundation of China (Grant Nos. 62335006, 62275065, 625B2063, 624B2050, 62405078, and 62505066), Natural Science Foundation of Heilongjiang Province (Grant Nos. BS2025F002 and LH2024F031), Heilongjiang Postdoctoral Fund (Grant Nos. LBH-Z23144 and LBH-Z24155), China Postdoctoral Science Foundation (Grant No. 2024M764172), Open Subject of Hebei Key Laboratory of Advanced Laser Technology and Equipment (HBKL-ALTE2025001), and the Fundamental Research Funds for the Central Universities (HIT.DZJJ.2025015 and HIT.NSFJG202463).

Author contributions

Yufei Ma proposed the original idea, developed the technical methodology, supervised the whole project, and revised the manuscript. Botao Liu designed the experimental framework, performed the investigations, established the experimental system, conducted the measurements, analyzed the data, and wrote the original manuscript. Guowei Han fabricated the piezoelectric ceramic tuning forks. Runqiu Wang, Xuan Yang, Haiyue Sun, Shunda Qiao, Ying He, Angelo Sampaolo, and Vincenzo Spagnolo contributed to the investigation and discussion.

Competing interests

Vincenzo Spagnolo serves as an Editor for the Journal, no other author has reported any competing interests.

Supplementary information

Supplementary information for this paper is available at
https://doi.org/10.29026/oes.2026.260068

Open Access This article is licensed under a Creative Commons Attribution 4.0 International License, which permits use, sharing, adaptation, distribution and reproduction in any medium or format, as long as you give appropriate credit to the original author(s) and the source, provide a link to the Creative Commons license, and indicate if changes were made. To view a copy of this license, visit http://creativecommons.org/licenses/by/4.0/
©The Author(s) 2026.
Published by Editorial Office of *Opto-Electronic Science*, Institute of Optics and Electronics, Chinese Academy of Sciences.

Opto-Electronic Journals Group
www.oejournal.org
Scan for Article PDF